Exploring uncommon Fe-oxides in non-metallic inclusions in ultra-high-strength steel

Results in Materials 23 (2024) 100598

Contents lists available at ScienceDirect

Results in Materials

journal homepage: www.sciencedirect.com/journal/results-in-materials

Exploring uncommon Fe-oxides in non-metallic inclusions in ultra-high-strength steel

Ekta Rani [a,*], Vandna K. Gupta [b], Francis Gyakwaa [c], Mourad Kharbach [a,d], Harishchandra Singh [a], Tuomas Alatarvas [c], Anna Martinelli [b], Timo Fabritius [c], Marko Huttula [a]

[a] Nano and Molecular Systems Research Unit, University of Oulu, P.O. Box 3000, Finland
[b] Department of Chemistry and Chemical Engineering, Chalmers University of Technology, 412 96, Gothenburg, Sweden
[c] Process Metallurgy Research Unit, University of Oulu, P.O. Box 3000, Finland
[d] Circular Economy/Sustainable Solutions, LAB University of Applied Sciences, Malekulana 19, 15101, Lahti, Finland

ARTICLE INFO

Keywords:
Low carbon steel
Non-metallic inclusion
Raman mapping
Principal component analysis
Fe-based oxides

ABSTRACT

Investigating non-metallic inclusions within ultra-high-strength-steel via conventional methods is a known: however, the challenge is to obtain chemical information of such inclusions at the sub-micrometer level. In this context, probing Fe-based oxide in inclusions is a vital aspect for guiding steel' performance. The vibrational properties of sub micrometer size Fe-based oxides were investigated by Raman mapping along with chemometric analysis with the aim of probing their chemical composition. Highly contrasted Raman spectra were recorded from several inclusions embedded at different spatial locations. The observed spectral features were identified as specific markers of hematite (α-Fe_2O_3) and magnetite (Fe_3O_4). Principal Component Analysis was used to confirm the presence of these markers and potentially revealing additional patterns. Their unambiguous assignment has been inferred by comparing our experimental findings with the literature data recorded either in single crystals of iron oxides or oxyhydroxides. Micro-Raman spectroscopy is proven to be a reliable, cost-effective, and non-invasive tool for the unambiguous identification of subsurface regions of steel.

1. Introduction

The remarkable mechanical strength of ultra-high-strength steel (UHSS), achieved through post-casting thermomechanical treatments, allows for the creation of lighter constructions with compact designs, thereby contributing to effective global warming control [1,2]. During the different stages of steel production, non-metallic inclusions (NMIs), such as sulfides (CaS, MnS), oxides, such as spinel ($MgAl_2O_4$) and calcium aluminates ($xCaO{\cdot}yAl_2O_3$) and nitrides (AlN, BN, TiN) form within the steel matrix [3]. These inclusions can significantly impact the steel's structural integrity, leading to unexpected failure modes [3]. In recent years, the focus has shifted towards understanding and characterizing these non-metallic inclusions at a microscopic level to unravel their influence on the mechanical properties of steel. Various non-destructive microscopic determinations and elemental specifications have already been employed to study NMIs [4–7]. Moreover, partially destructive electrolytic extraction to dissolve the steel matrix around an inclusion followed by imaging has been performed [8]. Conventional methods, however, fail to provide chemical information of such NMIs at the sub-micrometer level. Complications with chemical separations at the sub-micrometer scale within inclusions are another concern. Thus, a spectro-microscopic method with chemical sensitivity and good lateral resolution [9,10] is vital for studying the local variation of NMIs embedded within the steel matrix, especially. Recently, we employed non-destructive room temperature (RT) synchrotron-based X-ray absorption (XAS)-photoelectron emission microscopy (PEEM), referred to as X-PEEM [11], to study several selective NMIs.

The present study advances Raman mapping's merits to detect uncommon Fe-oxides that could be present on the surface of NMI within UHSS at the sub-micron level and brings in insightful surface approach to understand behavior of UHSS. Raman mapping is an innovative analytical technique that combines the power of Raman spectroscopy with high spatial resolution. Raman spectroscopy, based on the inelastic scattering of monochromatic light, offers a non-destructive means of probing vibrational modes within a material. Raman spectroscopy is advantageous for studying materials due to its ability to provide valuable insights into molecular composition, structure, and bonding without the need for extensive sample preparation. It offers non-

* Corresponding author.
E-mail address: Ekta.Rani@oulu.fi (E. Rani).

https://doi.org/10.1016/j.rinma.2024.100598
Received 21 March 2024; Received in revised form 23 May 2024; Accepted 19 June 2024
Available online 22 June 2024

destructive and non-invasive analysis, allowing researchers to examine materials in their native states. Additionally, Raman spectroscopy is versatile, capable of characterizing a wide range of materials, including solids, liquids, and gases, across various fields such as chemistry, physics, biology, and materials science. Its sensitivity to different vibrational modes enables the identification of chemical compounds, polymorphs, and phases, making it a powerful tool for both qualitative and quantitative analysis. Moreover, Raman spectroscopy can be coupled with imaging techniques to obtain spatially resolved information, enabling detailed mapping of samples and elucidation of heterogeneities. Overall, Raman spectroscopy stands out as a valuable technique for comprehensive and efficient material characterization. When applied to the study of Fe-oxides in non-metallic inclusions, Raman spectroscopy provides a wealth of information about their different crystalline phases. The integration of spatial mapping further enables researchers to visualize the distribution of these features within the steel matrix, offering unprecedented insights into the heterogeneity of the material.

While Raman mapping unveils the spatial distribution of Fe-oxides, the complex nature of these oxides demands a sophisticated approach for data analysis. Chemometrics, a field at the intersection of chemistry and statistics, provides the necessary tools to extract meaningful information from complex spectroscopic datasets. Principal Component Analysis (PCA) is a powerful technique commonly used to analyze complex data sets, including Raman mapping data. Raman mapping generates vast amounts of spectral data from different points across a sample, making it challenging to extract meaningful information efficiently. PCA helps in this regard by reducing the dimensionality of the data while retaining most of its variability. In Raman mapping, each spectrum represents a point in a high-dimensional space, with each dimension corresponding to a different Raman shift. PCA works by transforming this high-dimensional space into a new set of orthogonal axes called principal components. These components are ordered by the amount of variance they explain in the original data. By plotting the scores of the principal components, researchers can visualize the underlying trends or patterns present in the Raman mapping data. This visualization helps identify clusters, outliers, or correlations among spectral features that might not be immediately apparent in the original high-dimensional space. Thus, through techniques such as PCA and multivariate curve resolution (MCR), researchers can deconvolute the intricate Raman spectra, identifying individual components and their respective contributions. This not only aids in the identification of different Fe-oxide phases but also allows for a quantitative assessment of their relative concentrations. This work further employs the K-means clustering methods from vector quantization [12] to plot global chemical (in)homogeneities of involved oxides.

By employing Raman mapping coupled with advanced chemometric analyses, we seek to unravel the mysteries of uncommon Fe-oxides within non-metallic inclusions. The insights gained from this investigation are poised to guide the design and optimization of steel alloys, aiming to enhanced mechanical performance and reduced susceptibility to unexpected failure. Such a novel finding is hoped to help control behavior of UHSS in the future engineering paths.

2. Experimental section

The selected steel sample is commercial low-alloyed carbon steel with a nominal composition of 0.15 C, 0.3 Si, 1.0 Mn and 0.4 Cr, in wt.%.

Micro-Raman mapping measurements were performed in backscattering geometry at room temperature using an InVia Raman spectrophotometer from Renishaw equipped with an air cooled charged coupled device detector. During the measurements, the confocal mode and a × 100 long working distance Leica objective with a numerical aperture (NA) of 0.75 were used. With this experimental setup, a spectral resolution of ~1 cm^{-1} and a spatial resolution of about 0.8 μm (approximating to the relation 1.22·λ/NA, where λ is the wavelength of the incoming laser) could be achieved. The mapping measurements were performed with different values of the laser power varying it from 0.5 to 10 % of the source power (100 mW at the source). The Raman spectra were collected using the 532 nm laser as the excitation source. Before each measurement, the spectrophotometer was calibrated to the first-order vibrational mode of a Si wafer centering at 520.3 cm^{-1}.

PCA is a significant statistical technique in data analysis, known for its effectiveness in data and dimensionality reduction. It helps extract essential insights from complex datasets, revealing underlying patterns, correlations, and reducing noise. At its core, PCA transforms the original dataset into uncorrelated variables called principal components (PCs), capturing the dataset's key variance and facilitating understanding of its structure and characteristics [13]. In the domain of PCA, surface plots are powerful visualization tools that illustrate the complex relationships between data points and principal components. Each pixel in the plot represents a data point, with its position on the X and Y axes reflecting the values of two chosen principal components. The color or elevation of each pixel indicates the data point's position in the lower-dimensional space defined by these components. Surface plots help uncover clusters, patterns, or distinct groups in the dataset, providing researchers with a clearer understanding of its structure [14].

Loading plots in PCA serve as powerful tools, revealing the underlying influence of original variables, or features, on each principal component, thus unraveling profound insights. Each loading plot is intricately linked with a specific principal component and serves as a visual representation of the correlations existing between the original variables and the designated component. A high loading value, whether positive or negative, signifies the robust sway of a particular variable in shaping the direction and explaining the variance inherent to that specific component. Loading plots are, therefore, invaluable tools in decoding the essence of principal components and discerning which features harbor the utmost relevance in encapsulating the dataset's inherent variability [15].

For the structure of steel, Raman image data in general $\mathbf{X}$ (x × y × λ), is a 3-D array data cube, while x and y axes represent spatial information (pixels resolution) and the λ axis corresponds to the Raman spectral information. Our dataset comprised data from four distinct Raman spectroscopic measurements on four different inclusions, revealing variations in phonon frequencies across the 100-900 cm^{-1} range, along with differences in relative intensity and peak width in the spectra. To gain deeper insights, we conducted Raman spectroscopic measurements at various spatial positions within each inclusion, employing a spatial mapping approach that allowed us to explore how Raman spectra evolved across different points within the inclusions.

Thermodynamic software FactSage 8.2 with FSstel and FToxid databases selected was utilized to assess the solubility of Fe to known NMI phases. In addition to stoichiometric compounds, solutions liquid steel, austenite, ferrite, liquid slag, B-spinel, A-monoxide, corundum, $Ca_2(Al,Fe)_8SiO_{16}$, $Ca(Al,Fe)_{12}O_{19}$, $Ca(Al,Fe)_6O_{10}$, $Ca(Al,Fe)_4O_7$, $Ca(Al,Fe)_2O_4$, $Ca_2(Al,Fe)_2O_5$, and $Ca_3(Al,Fe)_2O_6$ were selected in the system. The amount and composition of NMI phases with decreasing temperature was calculated with the nominal steel composition (0.15 C, 0.3 Si, 1.0 Mn and 0.4 Cr, in wt.%.), assuming contents of 0.03Al, 0.002 Ca and 0.002 O in wt.%, allowing the formation of calcium aluminate-based oxide NMIs.

3. Results and discussion

This sample has been investigated in the authors' previous works [11,16]. The inclusions in the selected sample contain mainly Ca-based compounds, BN, and TiN. In the previous work, advanced Synchrotron X-ray absorption coupled with photoemission electron microscopy and first-principles calculations elucidated the structure, local bonding, and electronic properties of non-metallic inclusions (NMIs) in ultra-high-strength steel. Spectra analysis revealed the interaction mechanisms among NMIs and the steel matrix, with observations

suggesting preferential stabilization of Ca^{2+}-based phases through TiN and h-BN. In-situ spectro-microscopic determination using advanced Synchrotron X-ray absorption spectroscopy (XAS) coupled with photo-electron emission microscopy (PEEM) further investigated h-BN-containing inclusions, highlighting oxygen-substituted nitrogen defects and their influence on the material properties. These findings provide crucial insights for optimizing the interaction mechanisms among various inclusions and the steel matrix, guiding towards enhanced steel performance and cleaner production processes. Along with the observed markers for Ca-based inclusion, BN, and TiN, a signal corresponding to higher harmonics of Fe was noted in these studies, yet we were unable to determine its origin. This prompted us to explore a novel technique, Raman spectroscopy, which unexpectedly provided new information.

3.1. Raman mapping

Raman spectroscopic measurements performed on different inclusions showed variation in Raman spectra, i.e., different phonon frequencies within the region 100 - 900 cm^{-1}, varied relative intensity of peaks, and width of various peaks. To investigate the origin of these differences, we performed Raman spectroscopic measurements at spatially different positions in all the inclusions followed by many sets of Raman mapping (acquisition time 1 s) with step size ~0.15 μm on each inclusion to generate enough statistical data to make appropriate observations. Since Raman spectra show phonon frequencies in the range 200–800 cm^{-1} for all the inclusions, Raman images are generated using intensity of phonon with frequencies in the range 200–800 cm^{-1}. Representative optical and Raman images for these inclusions are given in Figs. 1–3, showing the corresponding Raman spectra for the marked positions in Figs. 1 b–3 b.

To distinguish various phases that are expected in inclusions, deconvolution of Raman spectra was carried out and fitting by Lorentzian lines was used. Fig. 4 shows typical fitted Raman spectra. The majority of the inclusions found in UHSS had Raman spectra similar to that shown in Fig. 4. Fig. 4a shows Raman bands at 217, 277, 386, 486, 586, 668, 712 and 801 cm^{-1}. Raman band at 486 and 801 cm^{-1} correspond to C_xA_y (possibly C3A or C12A7 [17]), and Boroxol ring [18], respectively. Fig. 4b shows Raman bands at 228, 252, 289, 389, 416, 502, 594, 618, 673, 717 and 813 cm^{-1}. Raman band at 502 and 813 cm^{-1} correspond to C_xA_y (C3A), and Boroxol ring, respectively. Similarly, Fig. 4c shows Raman bands at 235, 304, 395, 414, 504, 562, 614, 676, 712 and 815 cm^{-1}. Raman band at 504 and 815 cm^{-1} correspond to C_xA_y (C3A) and Boroxol ring, respectively. Fig. 4d also shows Raman bands at 222, 286, 390, 498, 599, 673, 714 and 812 cm^{-1}. Raman band at 498 and 812 cm^{-1} correspond to C_xA_y (could be CA or C12A7), and Boroxol ring, respectively.

As shown in Fig. 4, the Raman spectrum is mainly dominated by various oxides. A comparison with the literature [19] suggests the presence of various Fe-oxides, such as Goethite (α-FeOOH), Hematite (α-Fe_2O_3), Magnetite (Fe_3O_4) and Maghemite (γ- Fe_2O_3). One to one correspondence to particular Fe-based oxide phase is mentioned in Table 1. The room temperature Raman spectra show the expected bands associated to Fe-based oxides apart from peak observed at ~618 cm^{-1}, the origin of which shall be discussed later. A closer inspection of Fig. 4 and literature reveals that current data present different variation in the peak position.

Considering Fe_3O_4 (magnetite), crystallizing in an inverse cubic spinel structure, Fe ions exists in divalent (+2) and trivalent states (+3). Fe^{3+} ions are divided equally between the tetrahedral and octahedral sites, with the Fe^{2+} ions displaced to the remaining octahedral sites. As per group theory, the spinel structure consists of five Raman active vibrational modes: $A_{1g} + E_g + 3T_{2g}$. Reported values in the literature for these vibrations are 193 ($T_{2g}(1)$), 306 (E_g), 450–490 ($T_{2g}(2)$), 538 ($T_{2g}(3)$) and 670 cm^{-1} (A_{1g}) for the magnetite with A_{1g} as the most intense feature. The A_{1g} mode (670 cm^{-1}) of a ferrite is assigned to the motion of oxygen in the tetrahedral AO_4 group, involving symmetric stretching of an oxygen atom with respect to the metal ion in the tetrahedral void. Fig. 4 shows the observance of A_{1g} mode in the studied inclusions; however, Raman spectrum for Fe_3O_4 is either shifted to larger or smaller wavenumbers (Table 1). The observed changes in the Raman spectrum can be attributed to partial substitution of Fe^{3+} ions with other cations leading to structural changes [20–22]. As per our recent studies [11,16], it is known that within one NMI, there exist various phases such as, MnS, MgO–Al_2O_3, C_xA_y. Formation of these phases during steel processing can lead to interaction between different phases and thus possible substitution of Fe^{3+} ions with other metal cations such as Ca^{2+}, Mn^{2+}, Mg^{2+}. Comparison of the ionic radii of Ca^{2+}, Mn^{2+}, Mg^{2+}, and Fe^{3+} cations are 0.99, 0.82, 0.66 and 0.64 Å [20], respectively, shows that ionic radii of Ca^{2+} and Mn^{2+} cations is much larger than that of Fe^{3+} cation. In spinel ferrites, the ions present at tetrahedral site have a smaller radius than at the octahedral site. Thus, smaller ions prefer tetrahedral sites. Although the occupancy of Ca^{2+} and Mn^{2+} ions with large ionic radius would prefer the octahedral sites, it is reported that at low doping level, Ca^{2+} and Mn^{2+} ions can acquire tetrahedral sites and at higher concentrations substitute at octahedral sites [20]. Thus, substituting Fe^{3+} ions with Ca^{2+}, Mn^{2+}, and Mg^{2+} ions bring structural changes due to cation distribution in the spinel crystal lattice followed by changes in the lattice vibrations. The shifting of mode towards higher frequency (Fig. 4b–d) indicates the increase in the force constant due to the increase in strong bonding between the oxygen ions and substituted metal ion at the tetrahedral site. Moreover, substitution of the Fe ions by the lighter Ca or Mg ions will give rise to a higher frequency as compared to heavy Fe^{3+} ion. Shifted to different wavenumbers can be justified in terms of different distortions of the crystalline structure due to the presence of Ca^{2+} and Mg^{2+} ions with different atomic radius, mass, and bond lengths. In case of $Mn_xFe_{3-x}O_4$, the frequency of the A_{1g} mode is expected to decrease when substituting Mn for Fe in the T positions, due to both charge reduction and a larger cation-oxygen bond length [22], as observed in Fig. 4a. Different authors have also tried to find a correlation between the Raman shifts and the cation distribution of mixed spinels at the T and O sites, distinguishing two general behaviors for the A_{1g} mode: the appearance of the

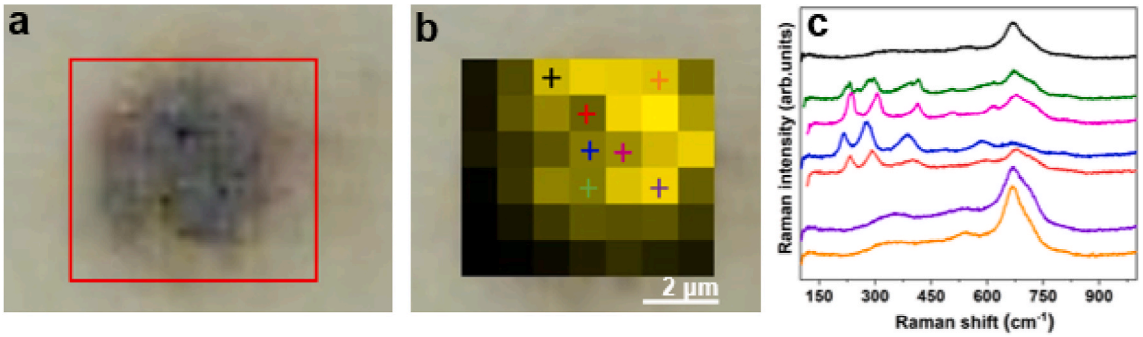

Fig. 1. Optical image of chosen inclusion (a), corresponding Raman image (b) and c) Raman spectra at marked locations in Raman image.

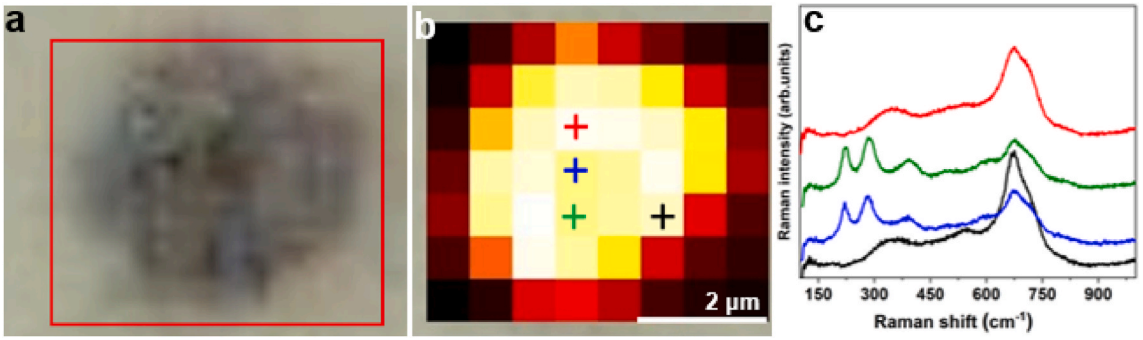

Fig. 2. Optical image of chosen inclusion I2 (a), corresponding Raman image (b) and c) Raman spectra at marked locations in Raman image.

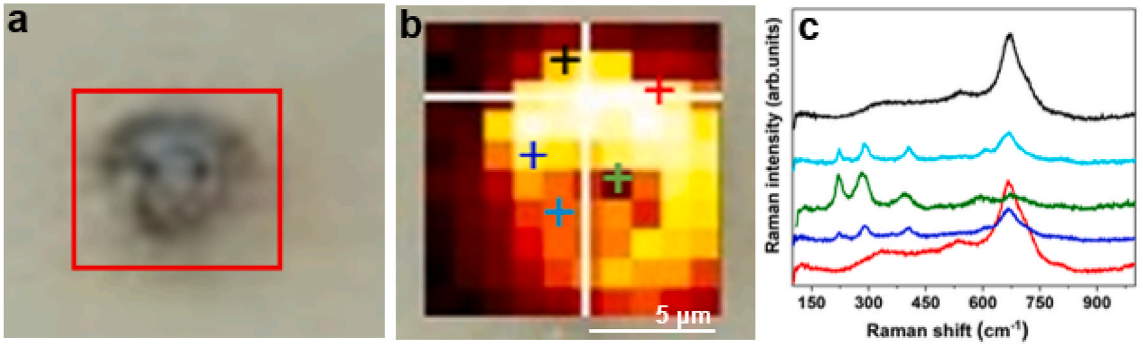

Fig. 3. Optical image of chosen inclusion I3 (a), corresponding Raman image (b) and c) Raman spectra at marked locations in Raman image.

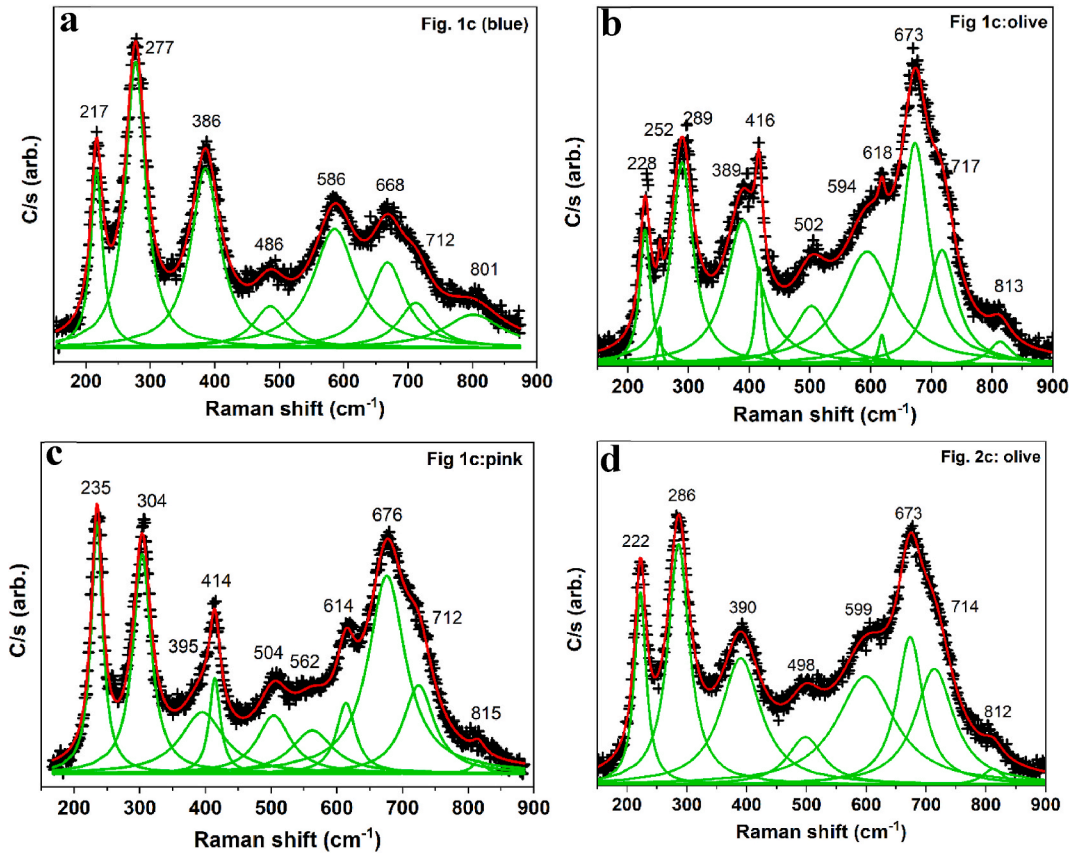

Fig. 4. Lorentzian line shape fitting of Raman spectra chosen from Figs. 1 and 2. Raw data are shown by symbols and solid line is fit to the data.

Table 1
Wavenumbers (cm^{-1}) of experimental Raman modes observed at room temperature, corresponding Fe-based oxide.

	Fig. 4a	Fig. 4b	Fig. 4c	Fig. 4d	Literature [19]
	Wavenumber (cm^{-1})				
Maghemite(γ-Fe_2O_3)	712	717	712	714	715
Magnetite (Fe_3O_4)	668	673	676	673	670
Wuestite (FeO)	586	594		599	595
Goethite (α-FeOOH)	386	389	395	390	385
Hematite (α-Fe_2O_3)	217,277	228,252,289,416	235,304,414	222,286	226,245,290,414

broadening of the band because of the vibration mode of two different cations (one-mode), or the emergence of two close peaks, each one belonging to two different vibration modes of two cations (two-modes). Accordingly, we can assign the peak at ~618 cm^{-1} and 670 cm^{-1} to the simultaneous presence of Mn^{2+} and Fe^{3+} ions at the tetrahedral sites as expected, considering the composition of both samples. Removal of degeneracy and appearance of shoulder with increasing other metal cation' concentration has also been observed owing to ordering of cations [20,22].

In hematite α-Fe_2O_3, isostructural with corundum α-Al_2O_3, Fe ions are disposed in pairs of $Fe(O)_6$ octahedra providing a trigonal sublattice. According to space group symmetry and factor group analysis, hematite has seven Raman-active vibrations ($2A_{1g}$ and 5_{Eg} modes) with most intense peak at ~290 cm^{-1} (E_g (2) + E_g (3)), along with other features at 225 (A_{1g}(1)), 247 (E_g(1)), 412 (E_g(4)), 498 (A_{1g}(2)) and 613 cm^{-1} (E_g (5)). A corroboration with our data suggests observance of peaks at 225, 247, 295, and 412 cm^{-1}. The observed blue shift in phonon frequency can be attributed to the insertion of another lighter and smaller cation such as, Al in the lattice [23] (in octahedral coordination: $r^{3+}_{Fe} = 0.64$ Å; $r^{3+}_{Al} = 0.53$ Å), a lowering of the average reduced mass is foreseen, and an induced strain due to the formation of shorter Al–O bonds with respect to Fe–O bonds is expected. In fact, it is known that the shortening of the interionic distance ($d_{Fe\text{-}O} = 2.09$ A° in α-Fe_2O_3; $d_{Al\text{-}O} = 1.97$ A° in α-Al_2O_3) is correlated to an increase of the force constants between pairs of ions. Both factors lead to a blue shift in the Raman spectrum of α-Fe_2O_3. A similar situation has been noted for Mg cation substation in α-Fe_2O_3 [24].

3.2. Raman mapping data with PCA decomposition

Raman spectroscopy proved to be an invaluable tool for investigating a wide range of inclusions, shedding light on their chemical and structural properties. Our primary goal in this study was to comprehend the sources of variation observed in the Raman spectra of these inclusions, all of which exhibited phonon frequencies within the 100–900 cm^{-1} range. Our investigation locates specific spectral features emerged as markers of Goethite (α-FeOOH), Hematite (α-Fe_2O_3), Magnetite (Fe_3O_4) and Maghemite (γ- Fe_2O_3). PCA played a pivotal role in confirming the presence of these markers and potentially revealing additional patterns related to different iron oxides or oxyhydroxides. To achieve this goal, we focused on generating Raman images that are created with phonon frequencies in the range of 100–900 cm^{-1}, implementing a data acquisition strategy that included multiple Raman mappings for each inclusion. This approach maintained the same spectral range while varying pixel sizes to ensure robust statistical analysis.

Regarding data organization, the Raman mapping data was structured as a three-way dataset, providing pixel-by-pixel information, with each pixel containing Raman spectra within the 100–900 cm^{-1} range. We then transformed this three-way data into a two-way dataset suitable for PCA. This transformation represented the data as a matrix, where each row represented a pixel, and each column represented Raman intensity at a specific wavenumber. Before applying PCA, a crucial data preprocessing step was implemented, encompassing baseline correction and normalization (autoscaling) to ensure data quality and reliability. PCA was subsequently applied to reduce data dimensionality and extract key features that distinguished inclusions based on their chemical composition. It transformed the data into a set of orthogonal variables, known as principal components (PCs), effectively capturing the maximum variance within the dataset. Following PCA analysis, we selected three PCs that explained significant variance within the data. Subsequently, the data was visualized in a lower-dimensional space, typically two dimensions, to explore how inclusions clustered based on their chemical composition. This visualization process aided in uncovering underlying patterns and relationships among the different inclusions. PCA results were instrumental in generating spatial distribution maps, offering visual insights into the distribution of various phases or compositions within the samples.

To simplify the complex spectral data, one-dimensional PCA was employed for each surface plot (Fig. 5(a–d)), reducing the data's dimensionality while preserving essential information captured by the most significant PCs. Consequently, we could explore how spectral information varied across the sample and its relationship with the three PCs. Regions (pixels) with similar spectral characteristics were clustered with the same color, enabling the identification of regions containing hematite or magnetite, and potentially other phases. These maps provided insights into the distribution of specific compounds like hematite and magnetite within the steel sample. For example, here PC1 typically represents variations related to the presence of specific phases such as Goethite (α-FeOOH) or Maghemite (γ-Fe_2O_3). PC2 captures variations associated with Hematite (α-Fe_2O_3) or Magnetite (Fe_3O_4). PC3 highlights additional variations or subtle differences in the composition or structure of iron oxides or oxyhydroxides. Subtle differences highlighted by PC3 in the data could include variations in the crystallinity, morphology, or stoichiometry of iron oxides or oxyhydroxides within the inclusions. These differences might manifest as shifts in peak positions, changes in peak intensities, or the emergence of new spectral features not prominently captured by PC1 or PC2. For example, PC3 might reveal differences in the degree of hydration or oxidation states of the iron oxide phases, indicating variations in the chemical environment or processing history of the inclusions. Additionally, PC3 could uncover nuances in the arrangement or orientation of crystalline structures within the inclusions, providing insights into their growth mechanisms or formation processes.

By projecting each pixel's Raman spectrum onto the three PCs, we captured the major variations in the spectral data. Loading plots, representing reduced spectra, were instrumental in identifying the wavenumbers or spectral features contributing most to each PC, helping to clarify dominant spectral variations. The loading plots (Fig. 5(e–h)) effectively separated regions with similar but distinct spectral features, indicating the presence of different phases or compositional variations, clarifying the dominant spectral variations captured by each PC. In loading plots, there are only three colors because each color represents one of the three principal components (PC1, PC2, or PC3), indicating the contribution of specific wavenumbers or spectral features to each PC. In contrast, surface plots show variations in spectral intensity across the sample, resulting in different colors representing different levels of intensity for each wavenumber. This variation in intensity leads to a more diverse range of colors in surface plots compared to loading plots.

The accuracy of our findings is further emphasized by validating PCA results through comparisons of spectral variations with known

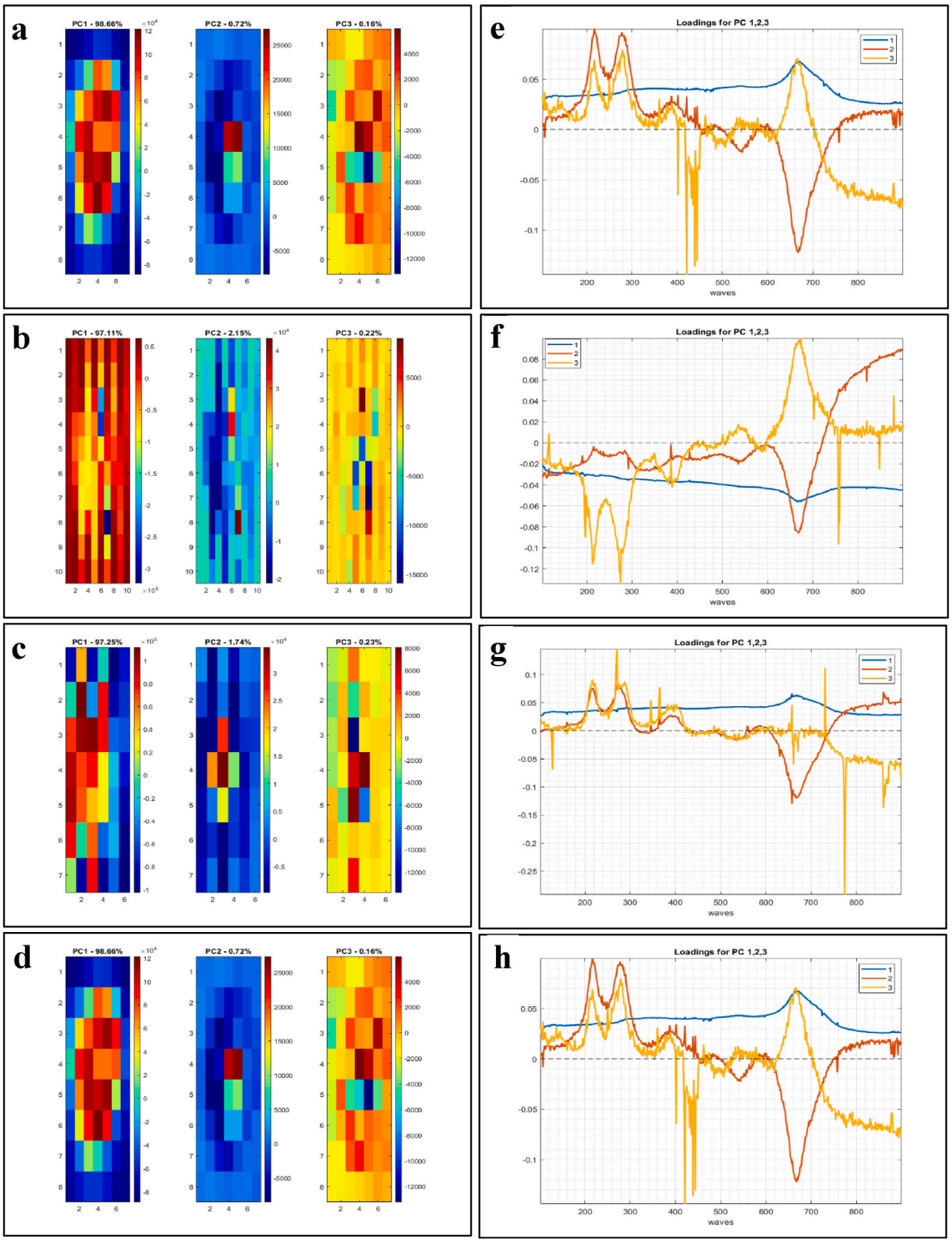

Fig. 5. PCA decomposition for Raman mapping data, (a–d) PCA Surface plots, (e–h) PCA loading plots.

characteristics of various Fe-oxides, such as Goethite (α-FeOOH), Hematite (α-Fe_2O_3), Magnetite (Fe_3O_4) and Maghemite (γ- Fe_2O_3), cross-referenced with established reference spectra (Table 1). This comprehensive approach deepened our understanding of the Raman spectra data and its underlying chemistry, not only confirming the presence of specific iron oxide phases but also revealing intricate patterns and the potential identification of additional chemical phases or variations within our sample.

In summary, the integration of spectral marker identification and PCA analysis greatly enhanced the accuracy of our findings. It not only confirmed the presence of specific iron oxide phases but also revealed intricate patterns and the potential identification of additional chemical phases or variations within our sample. Patterns observed in PC1 indicate the presence or distribution of specific Fe phases like Goethite or Maghemite within the NMIs. PC2 patterns provide insights into the distribution or variations of Hematite or Magnetite phases. Whereas PC3 patterns might reveal subtle differences or additional phases present in the NMIs, aiding in a more comprehensive understanding of their

composition and structure. This comprehensive approach provided a deeper understanding of the Raman spectra data and its underlying chemistry.

3.3. Thermodynamic assessment

The results of the thermodynamic calculations show the amount of NMI compounds in a steel mass of 100g (Fig. 6a), as well as the molar fraction of Fe in the stable compounds (Fig. 6b). At temperatures of 1600-1500 °C, molten slag is the dominant NMI phase, while the molar fraction of iron is in the range of 10^{-4}, which can be considered negligible. At lower temperatures, Ca_2SiO_4 is stable and as a stoichiometric compound it does not contain Fe. Solid solution calcium aluminates are stable with decreasing temperature, and as observed in Fig. 6b, the solubility of Fe is even lower than for liquid inclusions, further decreasing with lowering the temperature.

3.4. Discussion

Non-metallic inclusions in steel can be divided into endogenous and exogeneous ones, depending on their origin. Endogenous NMIs form in molten steel because of chemical reactions, such as aluminum deoxidation. Due to its high affinity to oxygen, aluminum is added to steel to decrease the total oxygen content in steel – by binding most of solute oxygen to Al_2O_3 NMIs and floating them to slag. When compared to iron, many other elements present in steel, such as Ca, Mg and Si have substantially higher affinity to oxygen. That is, the formation of CaO, MgO, and SiO_2 is more favorable than iron oxides within the molten steel during processing stages. Besides, one of the main targets for deoxidation is to prevent the formation of FeO in the steel [25]. It has been reported that iron oxide components may be present in the primary NMIs before deoxidation, but after Al addition the NMI composition transforms to phases such as calcium aluminates and spinel [26].

On the other hand, exogeneous NMIs originate from outside the molten steel, for instance refractory materials or steelmaking slags. Due to the steel flows in the mould during continuous casting, entrapped slag particles may end up as NMIs to the solidifying steel. Typically mould slag contains minor amounts of iron oxides; the pickup of FeO has been approximated to 1 % [27]. However, in addition to the slag main components CaO, SiO_2 and Al_2O_3, NMIs originating from the entrapped mould slag are characterized with Na and/or K [28,29]. Another source for iron oxides is reoxidation of steel during refining or casting. As pointed out by Cho et al. [30] reoxidation occurs when the deoxidized steel comes into contact with oxygen-containing phases such as air or reducible oxides in the slags. Utilizing SEM-EDS analysis, the authors detected hercynite ($FeAl_2O_4$) solid solution phases in Al-deoxidized steel samples with varying degrees of reoxidation. The laboratory-cast samples exhibited high FeO_n contents due to the experimental conditions. However, only a few NMIs in the samples obtained from a steel plant were categorized as hercynite. The authors concluded that after ruling out the specimen reoxidation after sampling, the presented SEM-EDS analysis method could be used to indicate the occurrence of steel reoxidation.

According to the thermodynamic calculation results, a decreasing solubility of iron oxides to calcium containing NMI phases is expected with decreasing temperature. That is, it is unlikely that the iron oxides observed in NMIs originate from the solid-state reactions between the steel matrix and the calcium based NMIs. For characterization and analysis of NMIs in steel, SEM-EDS can be considered the standard method. Iron is often excluded from the EDS analyses, as it is assumed to originate from the surrounding steel matrix rather than the NMI itself [31]. Finally, it cannot be ruled out that some material has accumulated on the NMI-steel matrix boundary, either in cavities or other topographical discontinuities on the polished surface. To conclude, iron oxide formation is more probable on the surface during sample preparation than in bulk material during steelmaking processes. Since Raman spectroscopy is a surface sensitive technique, one is able to probe uncommon Fe oxides in NMIs.

4. Conclusions

In the pursuit of understanding non-metallic inclusions within UHSS at the sub-micrometer scale, conventional methods have posed common challenges. However, this study underscores the significance of probing Fe-based oxides through the utilization of Raman mapping coupled with chemometric analysis. The results of this investigation reveal highly contrasted Raman spectra emanating from various inclusions positioned at different spatial locations within the steel matrix. Through rigorous analysis, these spectral features were unequivocally identified as specific markers of hematite (α-Fe_2O_3) and magnetite (Fe_3O_4), and PCA analysis greatly enhanced the accuracy of our findings. The unambiguous assignment of these spectral signatures was established by drawing comparisons with existing data in the literature obtained from single crystals of iron oxides or oxyhydroxides. The definitive proof of concept provided by this research not only enhances our understanding of the vibrational properties of Fe-based oxide but also showcases the practical value of Raman mapping in elucidating the chemical composition of these crucial subsurface features in commercial steel. Thus, this study contributes valuable insights that may pave the way for more informed engineering decisions, ultimately advancing the performance and reliability of ultra-high-strength-steel in diverse applications.

CRediT authorship contribution statement

Ekta Rani: Writing – review & editing, Writing – original draft, Investigation, Formal analysis, Data curation, Conceptualization.

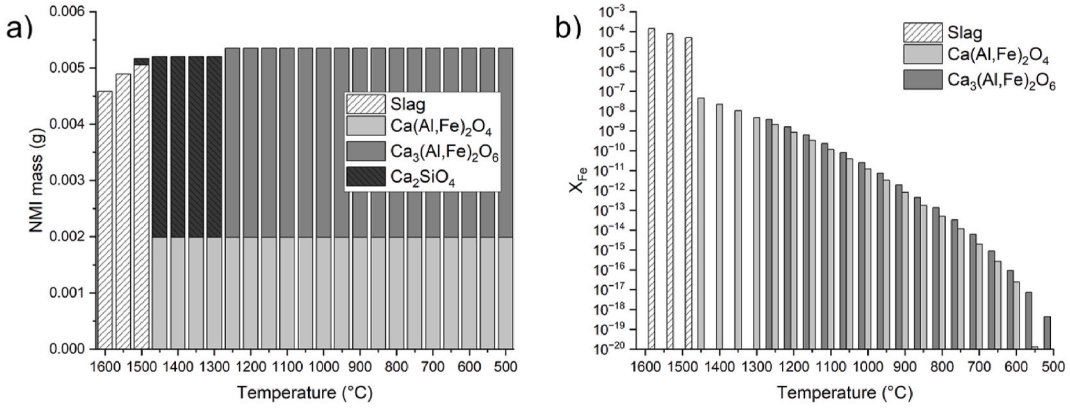

Fig. 6. Mass of stable NMIs as a function of temperature (a), and molar fraction of Fe in solution phases (b).

Vandna K. Gupta: Data curation. **Francis Gyakwaa:** Formal analysis, Data curation. **Mourad Kharbach:** PCA analysis and corresponsing writing. **Harishchandra Singh:** Formal analysis. **Tuomas Alatarvas:** Writing – review & editing, Resources. **Anna Martinelli:** Writing – review & editing, Funding acquisition. **Timo Fabritius:** Writing – review & editing, Funding acquisition. **Marko Huttula:** Writing – review & editing, Funding acquisition.

Declaration of competing interest

The authors declare that they have no known competing financial interests or personal relationships that could have appeared to influence the work reported in this paper.

Data availability

Data will be made available on request.

Acknowledgements

We acknowledge the University of Oulu & the Academy of Finland Profi 326291 (Profi5/HiDyn) and Profi 352788 (H2Future) in funding the current study. Funding from the Knut and Alice Wallenberg Foundation (Wallenberg Academy Fellowship award, 2016-0220) is also kindly acknowledged. HS also thanks Jane ja Aatos Erkon säätiö (JAES) and Tiina ja Antti Herlinin säätiö (TAHS) for their financial support on Advanced Steels for Green Planet project.

References

[1] Zhou, et al., Mater. Sci. Eng. 766 (2019) 138352.
[2] Zhou, et al., J. Mater. Res. Technol. 9 (2020) 8379–8390.
[3] Da Costa E. Silva, et al., J. Mater. Res. Technol. 8 (2019) 2408–2422.
[4] Suito, et al., ISIJ Int. 36 (1996) 528–536.
[5] Jung, et al., ISIJ Int. 44 (2004) 527–536.
[6] Imashuku, et al., Surf. Interface Anal. 51 (2019) 31–34.
[7] Bandi, et al., Ironmak. Steelmak. 47 (2020) 47–50.
[8] Janis, et al., Adv. Mater. Sci. Eng. 2014 (2014) 1–8.
[9] Rani, et al., J. Raman Spectrosc. 47 (2016) 457–467.
[10] Shi, et al., Small 14 (2018) 1–10.
[11] Singh, et al., Scr. Mater. 197 (2021) 113791.
[12] Kodinariya, et al., Int. J. 1 (2016) 90–95.
[13] Jolliffe, et al., Prison. Forced Labour Japan, 2019, pp. 1–17.
[14] Abdi, et al., Wiley Interdiscip. Rev. Comput. Stat. 2 (2010) 433–459.
[15] Jackson, et al., A Use's Guide to Principal Components, Wiley, 1991.
[16] Rani, et al., J. Mater. Res. Technol. 17 (2022) 2333–2342.
[17] Neuville, et al., Am. Mineral. 95 (2010) 1580–1589.
[18] Yadav, et al., RSC Adv. 5 (2015) 67583–67609.
[19] Giarola, et al., J. Raman Spectrosc. 43 (2012) 556–558.
[20] Kour, , et al.J. Indian, Pure Appl. Phys. 60 (2022) 742–753.
[21] Nakagomi, et al., J. Solid State Chem. 182 (2009) 2423–2429.
[22] Otero-Lorenzo, et al., Chem. Eur J. 22 (2016) 6666–6675.
[23] Tomislav Biljan, et al., J. Raman Spectrosc. 39 (2008) 40–46.
[24] Zhang, et al., J. Phys. Chem. C 125 (2021) 12893–12902.
[25] Verma N, Lind M, Pistorius PC, et al., 7 (2010) 189.
[26] Chi, et al., Steel Res. Int. 88 (2017) 1–10.
[27] Mills, et al., How Mold Fluxes Work, Elsevier Ltd., 2014.
[28] Ren, et al., Metall. Mater. Trans. B Process Metall. Mater. Process. Sci. 45 (2014) 1291–1303.
[29] Zhang, et al., Ironmak. Steelmak. 33 (2006) 129–139.
[30] Cho, et al., Metall. Mater. Trans. B Process Metall. Mater. Process. Sci. 55 (2024) 1337–1350.
[31] Nuspl, et al., Anal. Bioanal. Chem. 379 (2004) 640–645.